Journal of Physics G: Nuclear and Particle Physics

PAPER

Elastic scattering of ^{10}B + ^{119}Sn: optical model analysis at energies around the Coulomb barrier

To cite this article: W A Y Hatano *et al* 2025 *J. Phys. G: Nucl. Part. Phys.* **52** 075102

IOP Publishing Journal of Physics G: Nuclear and Particle Physics
J. Phys. G: Nucl. Part. Phys. **52** (2025) 075102 (13pp) https://doi.org/10.1088/1361-6471/adeda6

Elastic scattering of $^{10}B + ^{119}Sn$: optical model analysis at energies around the Coulomb barrier

W A Y Hatano[1], L R Gasques[1], V Scarduelli[1], L C Chamon[1], J K L Chaves[1], L M Martinis[1], G P Cessel[1], M A G Alvarez[2], J P Fernández-García[2] and L Garrido-Gómez[2]

[1] Universidade de Sao Paulo, Instituto de Fisica, Rua do Matao, 1371, 05508-090, Sao Paulo, SP, Brazil
[2] Departamento de Física Atómica, Molecular y Nuclear, Universidad de Sevilla, Apartado 1065, 41080 Sevilla, Spain

E-mail: lgasques@if.usp.br

Received 20 May 2025, revised 20 June 2025
Accepted for publication 9 July 2025
Published 25 July 2025

Abstract

This work investigates the elastic scattering of ^{10}B on ^{119}Sn at several energies around the Coulomb barrier. The experimental angular distributions are analyzed within the optical model framework using two different nuclear interactions: the São Paulo potential (SPP) and its updated version, SPP2. The analysis shows that SPP2 provides a better overall description of the data, with the main differences between the two interactions stemming from the matter density adopted for the ^{10}B projectile. The optical potentials obtained in this study are expected to serve as a reliable starting point for describing cross sections of other reaction channels for this system within the coupled-channel formalism.

Keywords: optical model, elastic scattering, nuclear potential

1. Introduction

The study of reactions involving weakly bound nuclei is essential for advancing our understanding of nuclear reaction dynamics. In this work, we investigate the $^{10}B + ^{119}Sn$ system at several bombarding energies around the Coulomb barrier, focusing on elastic scattering angular distributions. As a weakly bound nucleus, ^{10}B exhibits distinctive features arising

from its low binding energy ($^{10}\mathrm{B} \rightarrow {}^{6}\mathrm{Li} + {}^{4}\mathrm{He}$; $Q = -4.461$ MeV), which can give rise to reaction mechanisms that differ significantly from those associated with more tightly bound systems [1–6].

The central aspect of this work is the application of the optical model (OM) [7, 8] to analyze experimental elastic scattering angular distributions. Widely used in nuclear reaction studies, this framework has proven to be a powerful tool for describing the elastic process, as it enables a comprehensive treatment of both nuclear and Coulomb interactions. A systematic investigation using the OM can yield valuable insights into the underlying reaction mechanisms, including the role of surface effects and the interplay between nuclear and electromagnetic forces-both of which are particularly relevant for weakly bound systems [9–12]. While the OM provides a robust and simplified description of elastic scattering, it does not account for all possible reaction channels-particularly in systems involving weakly bound nuclei, where processes such as transfer and breakup may play significant roles.

To obtain a more comprehensive understanding of the reaction dynamics, coupled-channels calculations are often employed. This model explicitly includes couplings between different nuclear states, offering a more detailed and accurate representation of the underlying processes.

In this work, we present experimental angular distributions for the elastic scattering of ^{10}B on ^{119}Sn, measured at energies both below and above the Coulomb barrier. The cross-section calculations were performed within the OM framework. The main goal is to establish a solid foundation for future investigations that will incorporate more sophisticated approaches-such as coupled-channels methods-to further probe the complex dynamics of reactions involving weakly bound nuclei.

The paper is organized as follows: the experimental setup is described in section 2. The experimental results and OM analyses are presented in section 3. Finally, conclusions are drawn in section 4.

2. Experimental setup

The experiment was conducted at the Open Laboratory of Nuclear Physics and Applications (LAFNA), Institute of Physics, University of São Paulo, using an 8 MV electrostatic tandem accelerator. The ^{10}B beam was produced by a MC-SNICS ion source, and the ^{119}Sn target, with a thickness of approximately 50 μg cm^{-2}, was mounted at the center of the 30B scattering chamber. For normalization purposes, a thin layer of ^{197}Au (approximately 20 μg cm^{-2}) was evaporated onto the ^{119}Sn film. Three surface barrier detectors were mounted at sufficiently forward angles (30°, 40° and 50°) to ensure that the elastic scattering cross sections for ^{10}B on ^{119}Sn and ^{197}Au are predominantly governed by the Coulomb interaction. Consequently, these cross sections can be described using the well-known Rutherford formula. By imposing the condition that the ratio of the differential elastic scattering cross section to the Rutherford cross section equals one at these forward angles, a normalization factor was determined, allowing the scaling of the data over the full angular range.

Elastic scattering angular distributions for the $^{10}\mathrm{B} + {}^{119}\mathrm{Sn}$ system were measured at laboratory energies of $E_{\mathrm{Lab}} = 33.4$, 34.6, 35.5, 36.6, and 40.0 MeV. A small average energy loss of approximately 30 keV was estimated for the beam at the center of the composite target.

Particle identification was performed using the Silicon Telescopes Array for Reactions setup, based on measurements of energy loss (ΔE) and residual energy (E_{R}). Two 16×16

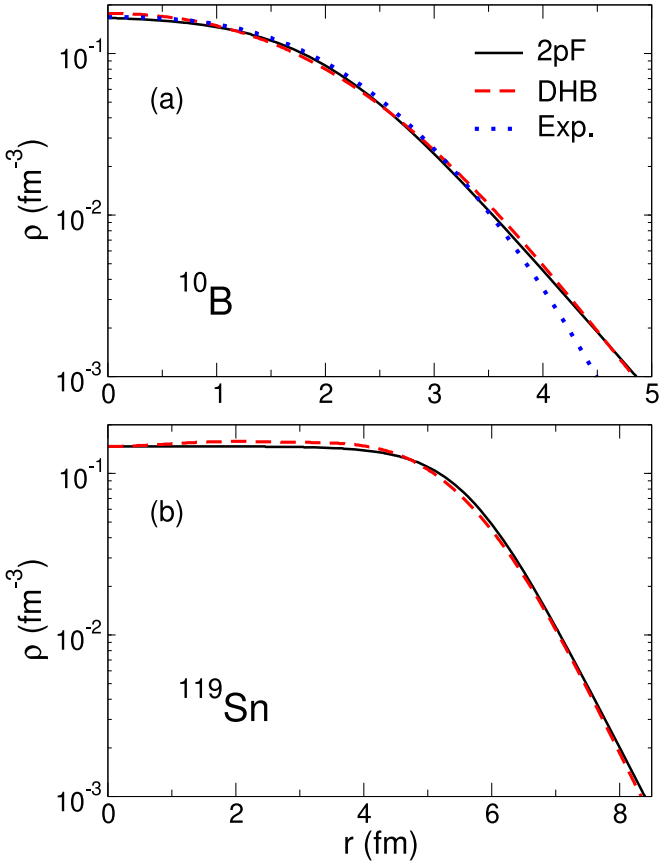

Figure 1. Matter densities for ^{10}B (a) and ^{119}Sn (b). Black solid, red dashed, and blue dotted lines correspond to the 2pF (SPP systematics), DHB (SPP2), and electron scattering-derived (SPP2) densities, respectively.

single-sided silicon strip telescopes with large active areas were mounted on a rotatable plate positioned approximately 12 cm from the target, each covering an angular range of about 22°. A detailed description of the array can be found in [13].

3. Results and analysis

We have performed OM calculations using two different models for the real part of the nuclear interaction: the São Paulo (SPP) [14, 15] and its updated version, SPP2 [16]. Both potentials are based on a double-folding procedure. The original SPP was developed to provide a global description of the nuclear interaction [14] and relies on an extensive systematization of nuclear densities parameterized by two-parameter Fermi (2pF) distributions. Although widely applied to the analysis of elastic and inelastic scattering, as well as transfer and fusion processes in heavy-ion reactions, the SPP does not account for specific nuclear structure effects in the average densities adopted in its systematics.

In contrast, the SPP2 is calculated using the REGINA code [16], which employs nuclear densities derived either from theoretical Dirac–Hartree–Bogoliubov (DHB) calculations [17] or from electron scattering data [18].

The 2pF-type densities used in the SPP systematics were obtained as averages over DHB-type calculations for a wide range of stable nuclei. Consequently, these densities are not expected to differ significantly from one another. Figure 1 shows the matter densities for ^{10}B (panel (a)) and ^{119}Sn (panel (b)), obtained from the SPP average systematics (black solid line) and from the DHB-based SPP2 calculations (red dashed line). As expected, the agreement between the two curves is satisfactory in both the interior and surface regions. However, for the ^{10}B nucleus, a marked discrepancy is observed between the 'experimental' matter density derived from electron scattering measurements (blue dotted line) and the results obtained using either the 2pF or DHB approaches. The implications of this difference will be discussed later in the manuscript.

In the present case, the SPP2 calculations employed the DHB density for ^{119}Sn and the experimental density for ^{10}B. The corresponding barrier heights in the laboratory frame are $V_{\rm B} \approx 35.2$ MeV for the SPP and $V_{\rm B} \approx 35.7$ MeV for the SPP2, indicating a difference of 0.5 MeV.

For the imaginary part of the optical potential, two approaches were considered: a phenomenological Woods–Saxon (WS) parametrization with $W_0 = 80$ MeV, $r_0 = 0.8$ fm, and $a_i = 0.30$ fm; or a potential obtained by multiplying the real part by a normalization factor N_i. With the chosen WS parameters, the imaginary potential is negligible in the surface region, accounting only for flux absorption due to barrier penetration, which is associated with the fusion process. In fact, the radius of this WS potential is $R_{i0} = 5.7$ fm, while the s-wave barrier radius is $R_{\rm B} = 10.2$ fm. We verified that moderate variations in the W_0 value do not alter the calculated cross sections. In contrast, the model employing N_i also includes surface absorption, which may be attributed to peripheral reactions.

Within the context of the OM, the elastic scattering data analysis was carried out using different combinations for the real and imaginary parts of the potential, as described below.

The so-called `OM1` approach combines the SPP or SPP2 for the real part of the optical potential with the WS potential for the imaginary part. Thus, the optical potential is given by

$$U_{\rm op.}(R) = V_N(R) - iW_0/\{1 + \exp[(R - R_0)/a_i]\}, \tag{1}$$

where $V_N(R)$ corresponds to the SPP or SPP2, and $R_0 = r_0 \times (A_1^{1/3} + A_2^{1/3})$ with A_1 and A_2 being the mass numbers of the projectile and target, respectively.

The `OM2` and `OM3` procedures adopt the same models for the real part of the nuclear interaction as in `OM1`, but modify the imaginary potential by multiplying the SPP or SPP2 by a factor N_i:

$$U_{\rm op.}(R) = V_N(R) + iN_i V_N(R). \tag{2}$$

In the `OM2` procedure, N_i is fixed at 0.78, following the systematics for imaginary potentials established in [19], whereas in `OM3`, N_i is treated as a free parameter, adjusted to better reproduce the experimental elastic scattering angular distributions.

In turn, the `OM4` procedure allows the simultaneous variation of two parameters, N_r and N_i, to achieve the best fit between the theoretical cross sections and the elastic scattering data. Thus, in this approach, both the real and imaginary parts of the OM potential can be adjusted:

$$U_{\rm op.}(R) = N_r\, V_N(R) + i\, N_i\, V_N(R). \tag{3}$$

We obtained the uncertainties of N_r and N_i from the data fits following the procedure described in [20].

It is worth noting that the `OM1` and `OM2` procedures involve no adjustable parameters. In `OM3`, a single parameter associated with the imaginary part of the potential is varied, while

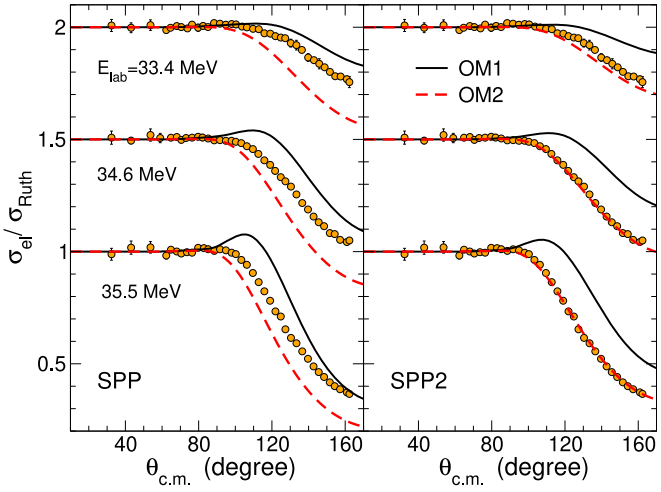

Figure 2. Elastic scattering angular distributions measured at bombarding energies below the Coulomb barrier. The curves represent the cross sections calculated using the `OM1` (black solid lines) and `OM2` (red dashed lines) procedures. The theoretical results were obtained assuming the SPP (left panel) and SPP2 (right panel). To avoid data overlap, some angular distributions have been vertically shifted by constant values.

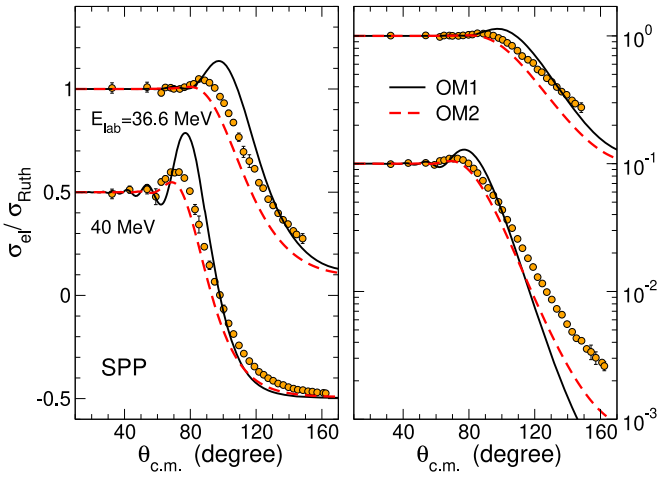

Figure 3. Elastic scattering angular distributions measured at bombarding energies above the Coulomb barrier. The curves correspond to OM calculations using the SPP. The black solid and red dashed lines represent the cross sections obtained with the `OM1` and `OM2` procedures, respectively. To avoid overlap, some angular distributions have been vertically shifted (linear scale, left panel) or divided (logarithmic scale, right panel) by constant factors.

`OM4` allows the adjustment of two parameters, one for the real part and another for the imaginary part.

As shown by the black solid lines in figure 2, the elastic scattering angular distributions measured at the three bombarding energies below the Coulomb barrier indicate that the `OM1` procedure provides a poor description of the data, regardless of whether the SPP (left panel)

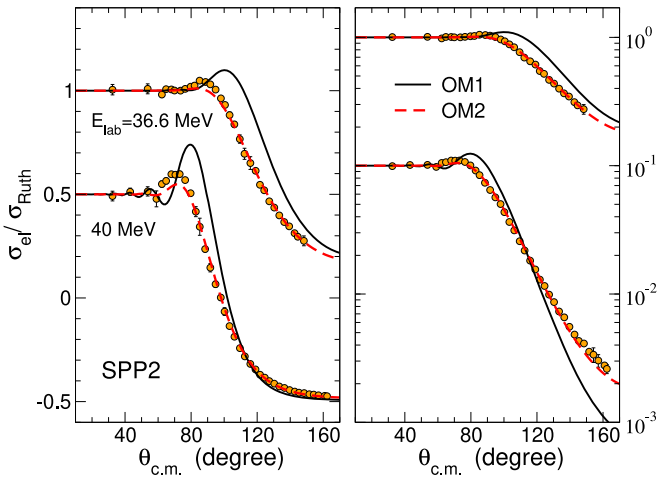

Figure 4. Same as in figure 3, but assuming the SPP2. To avoid overlap, some angular distributions have been vertically shifted (linear scale, left panel) or divided (logarithmic scale, right panel) by constant factors.

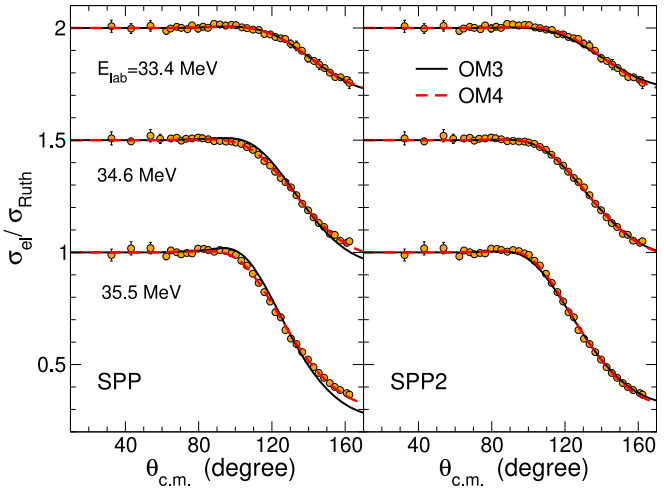

Figure 5. Same as in figure 2, but using the `OM3` (black solid lines) and `OM4` (red dashed lines) procedures. To avoid data overlap, some angular distributions have been vertically shifted by constant values.

or SPP2 (right panel) is used. This result is expected, as the presence of other reaction channels, such as inelastic excitations of the projectile and/or target, is not accounted for by an internally absorptive imaginary potential.

On the other hand, the SPP2 interaction yields much better agreement between data and theory when the internal imaginary potential is replaced by $W(R) = 0.78V_N(R)$ (`OM2` procedure). In contrast, the SPP within `OM2` leads to elastic scattering angular distributions that underestimate the experimental data (see figure 2).

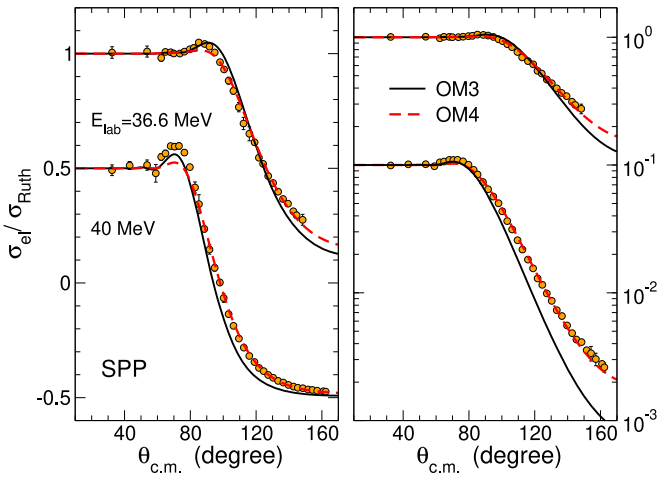

Figure 6. Same as in figure 3 (with SPP), but using the `OM3` (black solid) and `OM4` (red dashed) procedures. To avoid overlap, some angular distributions have been vertically shifted (linear scale, left panel) or divided (logarithmic scale, right panel) by constant factors.

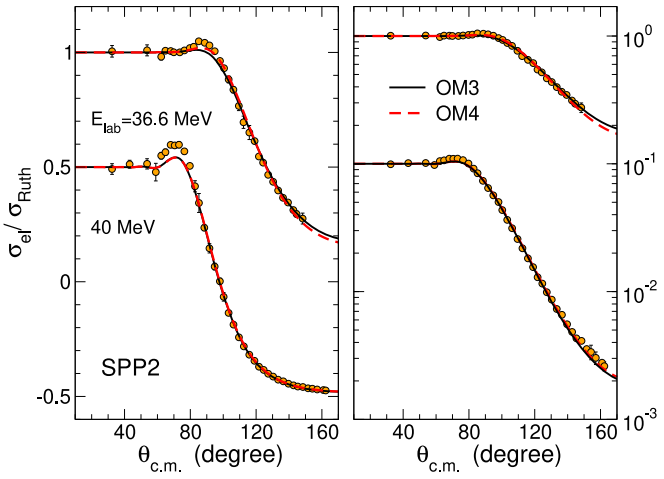

Figure 7. Same as in figure 4 (with SPP2), but using the `OM3` (black solid) and `OM4` (red dashed) procedures. To avoid overlap, some angular distributions have been vertically shifted (linear scale, left panel) or divided (logarithmic scale, right panel) by constant factors.

Throughout the manuscript, the elastic scattering angular distributions obtained at above-barrier energies are presented in both linear (left panel) and logarithmic (right panel) scales. This dual representation is important for highlighting the comparison between theoretical results and experimental data across different angular regions.

For the above-barrier energies, both procedures provide a poor description of the data across the entire angular range when the SPP interaction is used. The corresponding results are shown in figure 3, where the black solid and red dashed lines represent the `OM1` and `OM2` procedures, respectively. Figure 4 shows the results obtained using the SPP2 interaction, with

Table 1. Reduced chi-squared ($\chi^2_{\rm red}$) values obtained with the OM1 and OM2 procedures. For the SPP calculations, two-parameter Fermi (2pF) matter densities were assumed for both the projectile and the target. In the SPP2 case, the experimental density was adopted for ^{10}B and the theoretical DHB density was used for ^{119}Sn.

	SPP		SPP2	
E (MeV)	OM1	OM2	OM1	OM2
40.0	305	163	148	6.3
36.6	93	150	271	5.1
35.5	243	247	617	2.0
34.6	168	201	353	1.6
33.4	19	70	34	5.5

Table 2. Summary of the N_i and $\chi^2_{\rm red}$ values obtained from OM calculations using the OM3 procedure.

	SPP		SPP2	
E (MeV)	N_i	$\chi^2_{\rm red}$	N_i	$\chi^2_{\rm red}$
40.0	0.63 ± 0.14	159	0.87 ± 0.05	5.8
36.6	0.25 ± 0.03	22	0.76 ± 0.03	5.0
35.5	0.29 ± 0.02	15	0.79 ± 0.01	1.9
34.6	0.28 ± 0.01	6.1	0.72 ± 0.01	0.56
33.4	0.21 ± 0.01	0.36	0.53 ± 0.01	0.68

Table 3. Values of the parameter N_i, the correlation coefficient r, and the reduced chi-squared $\chi^2_{\rm red}$ obtained with the SPP model using the OM4 procedure, for each laboratory energy.

E (MeV)	N_r	N_i	r	$\chi^2_{\rm red}$
40.0	0.66 ± 0.02	0.60 ± 0.05	−0.71	8.2
36.6	0.83 ± 0.02	0.39 ± 0.02	−0.82	3.8
35.5	0.82 ± 0.01	0.43 ± 0.01	−0.88	1.6
34.6	0.82 ± 0.01	0.40 ± 0.01	−0.89	0.46
33.4	0.97 ± 0.02	0.23 ± 0.02	−0.88	0.34

the same line styles indicating the calculations for the OM1 and OM2 procedures. Overall, the OM2 procedure yields a significantly better description of the data compared to the results obtained with an internal imaginary potential (OM1).

The discrepancy between the experimental cross sections and those predicted by both models (SPP and SPP2) and procedures (OM1 and OM2) is quantified by the $\chi^2_{\rm red}$ values presented in table 1. As shown, although not always close to unity, the $\chi^2_{\rm red}$ values obtained with the combination of OM2 and SPP2 indicate an overall satisfactory description of the data.

By allowing the variation of a single parameter related to the imaginary potential (OM3), an improved description of the elastic scattering data is expected compared to the previously discussed analysis. Indeed, at energies below the Coulomb barrier, figure 5 shows excellent

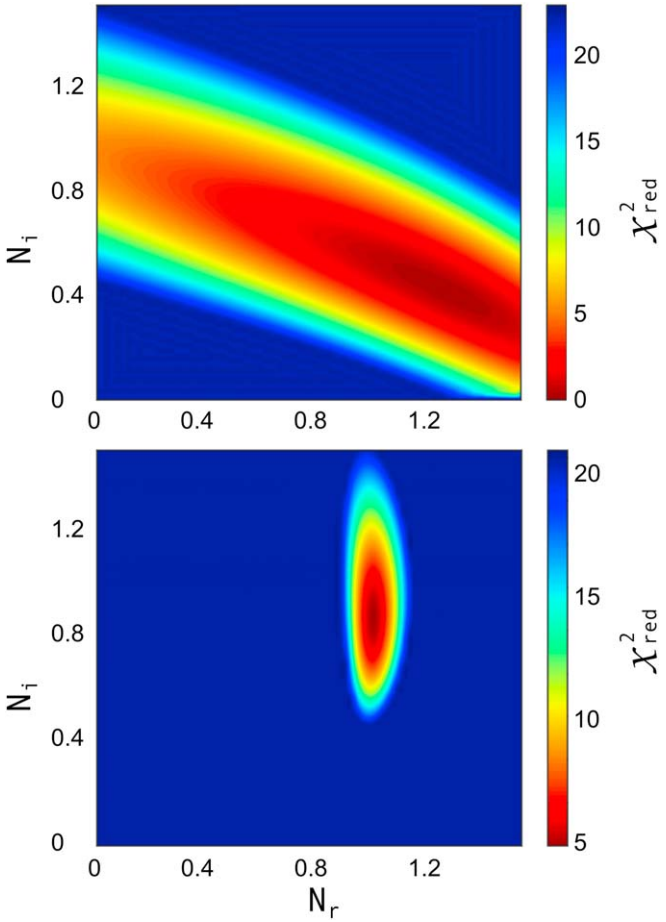

Figure 8. Reduced chi-square values ($\chi^2_{\rm red}$) as a function of the N_r and N_i parameters for $E_{\rm Lab} = 33.4$ MeV (upper panel) and $E_{\rm Lab} = 40$ MeV (lower panel). The results were obtained using the SPP2 interaction.

Table 4. The same as table 3, for the case of the SPP2.

E (MeV)	N_r	N_i	r	$\chi^2_{\rm red}$
40.0	0.98 ± 0.02	0.86 ± 0.08	−0.24	5.2
36.6	1.11 ± 0.02	0.62 ± 0.03	−0.77	2.7
35.5	1.08 ± 0.01	0.71 ± 0.01	−0.86	1.1
34.6	1.04 ± 0.01	0.70 ± 0.01	−0.89	0.49
33.4	1.23 ± 0.03	0.42 ± 0.02	−0.89	0.39

overall agreement between the calculated curves and the experimental data, regardless of whether the SPP or SPP2 interaction is used.

However, a closer inspection of the left panel in figure 5 shows that the OM3 procedure has limitations. In particular, adjusting only N_i fails to satisfactorily reproduce the data at very

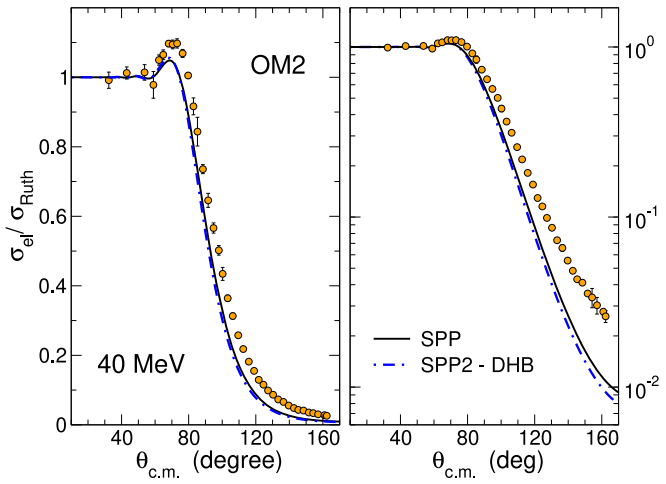

Figure 9. Elastic scattering angular distribution measured at $E_{\rm Lab} = 40$ MeV. The black solid line corresponds to the calculation using the SPP interaction, while the blue dot–dashed line was obtained with the SPP2 interaction, employing the DHB density distribution for the ^{10}B projectile. The left and right panels show the results in linear and logarithmic scales, respectively. Note that neither SPP nor SPP2 with DHB for ^{10}B matches the data well, highlighting the importance of empirical densities.

backward angles for the angular distribution measured at $E_{\rm Lab} = 35.5$ MeV with the SPP interaction. This limitation is addressed in the OM4 procedure by introducing an additional parameter, N_r, which enables the rescaling of the real part of the potential. This adjustment allows the SPP to effectively emulate the SPP2 interaction, resulting in better agreement with the experimental data.

At above-barrier energies, figure 6 shows that the SPP does not provide a satisfactory description of the data when only N_i is adjusted. On the other hand, when the OM4 procedure is adopted-where both N_r and N_i are simultaneously adjusted-the SPP interaction provides a generally good description of the elastic scattering data. However, the agreement between the theoretical results and the experimental data shows increasing discrepancy in the angular region where the Coulomb and nuclear forces interfere.

As shown in figure 7, both the black solid (OM3) and red dashed (OM4) lines are in good agreement with the data obtained at bombarding energies above the Coulomb barrier. These results correspond to OM calculations using the SPP2 for both the real and imaginary parts of the nuclear potential.

Table 2 presents the adjusted N_i values obtained from SPP and SPP2 OM calculations performed within the OM3 procedure. The corresponding $\chi^2_{\rm red}$ values indicate that, while the SPP interaction provides a satisfactory fit to the elastic scattering data at below-barrier energies, the theoretical cross sections fail to adequately describe the data at bombarding energies above the Coulomb barrier. In contrast, the SPP2 OM calculations yield a good description of the elastic scattering data over the entire energy range.

Tables 3 and 4 present the values of N_r, N_i and $\chi^2_{\rm red}$ obtained from the OM4 fitting procedure using the SPP and SPP2, respectively. As expected, the $\chi^2_{\rm red}$ values demonstrate that the simultaneous variation of both parameters leads to an excellent description of the elastic scattering data, regardless of the chosen nuclear interaction.

The variation of the reduced chi-square values as a function of the N_r and N_i parameters is shown in figure 8 for both the lowest and highest measured energies. These results were obtained using the SPP2 interaction. As seen in the upper panel of the figure, corresponding to $E_{\rm Lab} = 33.4$ MeV, a strong correlation between the two parameters is evident. The fitting analysis reveals a relatively broad region in the (N_r, N_i) parameter space that yields satisfactory results, suggesting that the fit quality remains stable under moderate variations of both parameters within this region. In contrast, for $E_{\rm Lab} = 40$ MeV, shown in the lower panel of figure 8, the values of N_r are tightly clustered around unity, while a wide range of N_i values still leads to a good description of the elastic scattering data.

Given these arguments, one might conclude that the uncertainty in N_r at $E_{\rm lab} = 33.4$ MeV should be significantly larger than at $E_{\rm lab} = 40$ MeV, and that the uncertainties in the parameter N_i should be similar at both energies. However, this conclusion may be misleading, as such behavior is not actually observed in table 4, where the uncertainties were calculated according to the method presented in [20]. Indeed, except for the case at 40 MeV, the N_r values for SPP2-OM4 presented in table 4 are not compatible with unity within uncertainties. On the other hand, the SPP2-OM3 results, which assume $N_r = 1$, are quite satisfactory and very similar to those of SPP2-OM4, as shown in figures 5 and 7. Altogether, this illustrates the challenges associated with assigning uncertainties in analyses of this nature.

At all measured energies, a strong inverse correlation between the parameters N_r and N_i is observed: as one increases, the other decreases. This reflects a clear negative correlation, where variations in one parameter are consistently offset by opposing variations in the other. This behavior is further corroborated by the negative correlation coefficients, r, presented in tables 3 and 4. In particular, as shown in table 4 and in the lower panel of figure 8, the correlation is noticeably weaker only in the case of SPP2 at 40 MeV.

Note in table 4, for the SPP2 interaction, that the N_r values are close to unity, while the N_i values remain near the standard value $N_i = 0.78$, obtained from the systematics of imaginary potentials reported in [19]. An exception is observed at $E_{\rm Lab} = 33.4$ MeV. Due to the absence of adjustable parameters, the OM2 procedure ($N_r = 1$ and $N_i = 0.78$) represents a genuine prediction rather than a fit to the data. Indeed, inspection of figures 2 and 4 shows that the SPP2, within the standard OM2 procedure, provides a good description of the data at all energies—including those at $E_{\rm Lab} = 33.4$ MeV.

The difference between the results obtained with SPP and SPP2 is primarily associated with the matter density adopted for the ^{10}B projectile. While the SPP employs a 2pF density resulting from a systematic parameterization, the SPP2 was applied here with the experimental matter density for ^{10}B. To illustrate this point, figure 9 shows the elastic scattering cross sections calculated within the OM2 procedure, this time using the DHB density for the ^{10}B projectile in the SPP2 framework (blue dot-dashed line). The comparison with the result obtained using SPP (black solid line) reveals good agreement between the two calculations, although neither provides a satisfactory description of the experimental data. This clearly indicates that adopting a realistic density distribution for the ^{10}B projectile is essential for achieving a reliable description of the elastic scattering data.

4. Conclusion

In this work, we investigated the elastic scattering of ^{10}B on ^{119}Sn at several energies around the Coulomb barrier. The experimental angular distributions were analyzed within the OM framework, employing two nuclear interactions: the SPP and its updated version, SPP2. Four

distinct procedures were applied, enabling a systematic exploration of the effects of independently varying the real and imaginary parts of the optical potential.

Between the two interactions, SPP2 provided a consistently better description of the elastic scattering data. This improvement stems primarily from the matter density adopted for the ^{10}B projectile, rather than from differences in the effective interaction itself. In particular, SPP2 incorporates a more accurate density profile derived from electron scattering data, leading to improved agreement with the experimental results. Moreover, calculations performed with SPP2 using fixed parameters within the `OM2` procedure demonstrated its predictive power, yielding good results at all energies.

These findings underscore the importance of employing realistic nuclear densities and interaction forms in OM analyses. The results presented here establish a robust foundation for future studies employing more advanced approaches-such as coupled-channel or few-body methods-which are expected to offer deeper insights into the reaction dynamics of the $^{10}\mathrm{B} + {}^{119}\mathrm{Sn}$ system. Coupled-channel calculations are currently in progress including inelastic excitation of the projectile and target, as well as transfer processes. The corresponding results will be presented in a forthcoming publication.

Acknowledgments

This work has been partially supported by Coordenação de Aperfeiçoamento de Pessoal de Nìvel Superior (CAPES) Proc. No 88887.834953/2023-00, Fundação de Amparo à Pesquisa do Estado de São Paulo (FAPESP) Proc. No 2019/07767-1, 2021/11425-9, 2022/09060-5, 2024/01416-0, Conselho Nacional de Desenvolvimento Cientìfico e Tecnológico (CNPq) Proc. No 302544/2022-4, 302072/2022-5, 315864/2023-0, and project INCT-FNA Proc. No 464898/2014-5. This work has also been partially supported by the Spanish Ministerio de Economìa y Competitividad and FEDER funds (PGC2018-096994-B-C21), and by the project PAIDI 2020 with reference P20 01247, funded by the Consejerìa de Economìa, Conocimiento, Empresas y Universidad, Junta de Andalucìa (Spain) and by 'ERDF A way of making Europe'. This work is part of the project supported by the Spanish Ministerio de Ciencia, Innovación y Universidades (PID2023-146401NB-I00). This work has been partially supported by Ministerio de Universidades, project REC-B-22289-1. This work has been developed within the context of the IReNA (International Research Network for Nuclear Astrophysics) and the IANNA (Ibero-American Network of Nuclear Astrophysics). The authors acknowledge all support and collaboration from IReNA and IANNA (National Science Foundation under Grant No. OISE-1927130).

Data availability statement

All data that support the findings of this study are included within the article (and any supplementary files).

Author contributions

W A Y Hatano 0000-0002-4650-3098
Formal analysis (lead), Investigation (equal)

L R Gasques 0000-0002-0963-1816
Formal analysis (equal), Writing – original draft (equal)

V Scarduelli 0000-0002-9993-0659
Investigation (equal), Supervision (equal)

L C Chamon 0000-0001-9624-0882
Investigation (equal), Writing – review & editing (equal)

J K L Chaves 0000-0001-6070-7997
Investigation (equal)

L M Martinis 0009-0006-3815-2052
Formal analysis (equal)

G P Cessel 0000-0003-2425-8711
Formal analysis (equal)

M A G Alvarez
Writing – review & editing (equal)

J P Fernández-García 0000-0001-7798-5678
Formal analysis (equal), Writing – review & editing (equal)

L Garrido-Gómez 0000-0002-7553-490X
Formal analysis (equal), Writing – review & editing (equal)

References

[1] Gasques L R, Hinde D J, Dasgupta M, Mukherjee A and Thomas R G 2009 *Phys. Rev. C* **79** 034605
[2] Gasques L R *et al* 2018 *Phys. Rev. C* **97** 034629
[3] Gasques L R *et al* 2020 *Phys. Rev. C* **101** 044604
[4] Aversa M *et al* 2020 *Phys. Rev. C* **101** 044601
[5] Gasques L R *et al* 2021 *Phys. Rev. C* **103** 034616
[6] Nassurlla M *et al* 2024 *Universe* **10** 51
[7] Feshbach H *et al* 1958 *Annu. Rev. Nucl. Part. Sci.* **8** 49
[8] Dickhoff W H *et al* 2019 *Prog. Part. Nucl. Phys.* **105** 252
[9] Gasques L R *et al* 2004 *Phys. Rev. C* **69** 034603
[10] Alvarez M A G *et al* 2019 *Phys. Rev. C* **100** 064602
[11] Bhattacharjee S *et al* 2022 *Phys. Rev. C* **106** 064612
[12] Garrido-Gómez L *et al* 2024 *Phys. Rev. C* **109** 054608
[13] Martinis L M *et al* 2025 *Phys. Rev. C* **111** 034615
[14] Chamon L C *et al* 2002 *Phys. Rev. C* **66** 014610
[15] Gasques L R 2021 *Braz. J. Phys.* **51** 269
[16] Chamon L C, Carlson B V and Gasques L R 2021 *Comput. Phys. Commun.* **267** 108061
[17] Carlson B V and Hirata D 2000 *Phys. Rev. C* **62** 054310
[18] Vries D D, Jager C W D and Vries C D 1987 *Atomic Data Nucl. Data Tables* **36** 495
[19] Alvarez M A G *et al* 2003 *Nucl. Phys. A* **723** 93
[20] Abriola D, Arazi A, Testoni J, Gollan F and Martì G V 2015 *J. Phys.: Conf. Ser.* **630** 012021